THE JOURNAL OF PHYSICAL CHEMISTRY C

pubs.acs.org/JPCC Article

New Data-Driven Interacting-Defect Model Describing Nanoscopic Grain Boundary Compositions in Ceramics

Xiaorui Tong, William J. Bowman, Alejandro Mejia-Giraldo, Peter A. Crozier, and David S. Mebane*

Cite This: J. Phys. Chem. C 2020, 124, 23619–23625 Read Online

ACCESS | Metrics & More | Article Recommendations | Supporting Information

ABSTRACT: A data-driven, interacting-defect model for inhomogeneous systems has quantitatively described the nanoscopic composition of high solute concentrations at grain boundaries in ion-conducting ceramics. The data-driven Cahn–Hilliard model was applied to high-spatial-resolution composition data gathered at grain boundaries in calcium-doped ceria. The statistical methodology for the data-driven procedure shows definitively that an inhomogeneous thermodynamics approach (gradient terms) is required to quantitatively describe the local grain boundary composition. The model additionally shows coaccumulation of negatively charged acceptor dopants and positively charged oxygen vacancies at the interface, which is qualitatively in accordance with atom probe tomography evidence in acceptor-doped ceria. The reported model is the first to quantitatively explain microscopic experiments in ion-conducting ceramics.

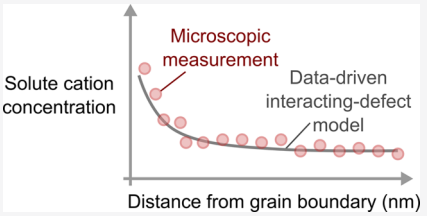

INTRODUCTION

Electroceramics are of great technological importance due to their role in applications such as solid oxide fuel cells,[1] electrolyzers,[2] solid-state batteries,[3] sensors,[4] mechanical actuators,[5] and next-generation electronic applications such as resistive switching memory.[6] The properties of these materials are generally determined by interfaces (especially grain boundaries) and surfaces, in the vicinity of which—in the so-called "space-charge" zone—the concentrations of chemically active, charge-carrying species (point defects) can differ significantly from the bulk crystal due to thermodynamically driven accumulation or depletion.[7,8] Despite the importance of this phenomenon, no consensus has emerged on a quantitative model framework for space-charge zones in materials with nondilute concentrations of charged defects[9−12] (approximately greater than 1% site occupancy[13]), a category that encompasses a majority of ion conductors of technological interest. The multiscale nature of the space-charge phenomenon (in which a nanoscopic interface region exists in equilibrium with a macroscopic bulk phase) means that continuum models are necessary to properly describe the thermodynamics outside of exclusively nanoscale situations. Moreover, if we are to leverage our thermodynamic understanding/interpretation of interfacial properties to realistic polycrystalline materials comprising many (hundreds to tens-of-thousands) interface types and/or variants, computationally efficient models will be required. Such models will be critical to interpreting high-throughput experimental measurements and fully utilizing correlated multiscale data acquisition methods focused on probing statistically significant numbers of grain boundaries.[14]

Until recently, the only quantitative continuum treatments available have been models based on the Poisson–Boltzmann (PB) approximation, as introduced by Gouy.[15] The PB approximation holds absolutely in the limit of infinite dilution, and PB-based "space-charge" theories have successfully described interfacial and grain boundary conductivity in dilute ionic conductors. There are two principal variants: the "Gouy–Chapman" model allows for nonuniform concentrations of all charge carriers, while the "Mott–Schottky" formulation assumes that one or more charge carriers are fixed and spatially uniform in concentration.

While Mott–Schottky and Gouy–Chapman models have been highly successful for dilute-solution electroceramics, there is a growing body of experimental evidence[16−25] and theoretical predictions[22,26] that confirm defect concentrations at GBs which exceed the range of validity of the dilute-solution assumption. These observations are not surprising considering the typical temperatures employed for ceramic processing. There is a strong driving force for solute segregation to reduce the overall system energy due to cation size mismatch, electrostatic forces (i.e., GB core charge neutralization), and reduction in the GB energy.[9,16,21,27,28] The ionic conductivity behavior of GBs with high solute concentration is often quite different from the predictions of the dilute solute models.[14,29] A recent example is Ca-doped CeO_2; there the GB conductivity increased by 4 orders of magnitude when the GB Ca molar concentration increased from 20 to 40%,[29] contradicting dilute-case space-charge models, which predict vanishing space-charge regions at concentrations well below

Received: June 23, 2020
Revised: September 1, 2020
Published: October 20, 2020

https://dx.doi.org/10.1021/acs.jpcc.0c05713
J. Phys. Chem. C 2020, 124, 23619–23625

20%. PB models are nonetheless frequently employed to interpret macroscopic measurements (such as conductivity) in concentrated systems.[21,30−34]

To move beyond dilute-solution models, treatment based on the Cahn−Hilliard theory[35] of inhomogeneous systems—the "Poisson−Cahn" (PC) theory, introduced in 2015[9,36]—quantitatively replicated macroscopic conductivity data while qualitatively replicating microscopic observations in concentrated systems. A subsequent study showed quantitative agreement with X-ray photoelectron spectroscopy measurements of surface defect concentrations in acceptor-doped ceria,[37] but until now, no continuum model had shown quantitative correspondence with microscopic measurements of defect concentrations as a function of distance from a surface or interfaced in a concentrated solid solution.

This article reports the first continuum model to achieve such quantitative correspondence to microscopic observations of defect concentration profiles in the immediate vicinity of a grain boundary. A Bayesian data-driven model-building method was used to construct the functional form of the excess, inhomogeneous free energy directly from the microscope data. The microscopic data set was obtained from numerous measurements made on grain boundaries in calcium-doped ceria using electron-energy loss spectroscopy (EELS) in an aberration-corrected scanning transmission electron microscope (STEM).

The work shows, in a statistically rigorous manner, that the space-charge model must utilize thermodynamic models for inhomogeneous systems to successfully replicate the microscopic data set. The data-derived model additionally shows coaccumulation of oppositely charged defects (calcium dopant cations and oxygen vacancies) in the space-charge zone, qualitatively replicating a surprising observation recently made in neodymium-doped ceria with atom probe tomography.[25] The application of the data-driven approach to the experimental data set is effectively a measurement of the inhomogeneous excess free energy of the system.

COMPUTATIONAL METHODS

Physical Model. The basis of the physical model is the formulation for the free energy functional

$$\mathcal{F}[y, v, \varphi] = \int_{\partial\Omega} \Phi(\partial y, \partial v) + \int_{\Omega} \{\eta(y, v, \nabla y, \nabla v) + nk_{\mathrm{B}}T[y \log y + v \log v + (1 - y) \log(1 - y) + (1 - v) \log(1 - v)] + \rho(y, v)\varphi - \epsilon|\nabla\varphi|^2\} \quad (1)$$

where Ω is a domain corresponding to the electrolyte system with $\partial\Omega$ its boundary at the interface; y and v are functions defined on Ω quantifying site fractions of ionized acceptor dopants and oxygen vacancies, respectively; Φ is a function describing the interfacial thermodynamics in terms of the boundary concentrations of y and v; n is a site density; ρ is a charge density; φ is the electrostatic potential; ϵ is the permittivity; and η is the interaction term (or "excess free energy") of the inhomogeneous system.

Minimization of the free energy functional is subject to the constraint of the conservation of mass in the system as shown in equations3

$$\int_{\Omega} (v - \overline{v}) = 0 \quad (2)$$

$$\int_{\Omega} (y - \overline{y}) = 0 \quad (3)$$

where $\overline{y}$ and $\overline{v}$ are the average dopant and vacancy site fraction in the material. These constraints are added to the function using Lagrange multiplier λ_y and λ_v. The resulting Euler−Lagrange equations are given in the Supporting Information.

The model considers dopant cations and oxygen vacancies as the sole defects in the system. The solution of the model equations yields defect profiles as a function of distance from the interface for defect concentrations and electrostatic potential.

Data-Driven Model Building. The vehicle for data-driven model building in framework 1 is the inhomogeneous excess free energy function η. This function is written in formal in terms of Gaussian process (GP) stochastic functions of the BSS-one-way analysis of variance (ANOVA) form[38,39]

$$\eta(y, v, \nabla y, \nabla v) = \delta_l(y, v) + \delta_{cy}(y)|\nabla y|^2 + \delta_{cv}(v)|\nabla v|^2 \quad (4)$$

where the δ terms are BSS-ANOVA GPs. Each of the GPs is first decomposed into terms corresponding to the effects of each input, individually then as pairs of two—i.e., main effects and two-way interactions, physically corresponding to self-interactions (dopant−dopant or vacancy−vacancy) and cross-interactions (dopant-vacancy). Terms for each interaction are then decomposed in a Karhunen−Loéve expansion

$$\delta_l(y, v) = \beta_0 + \sum_i \beta_{y,i}\phi_i(y) + \sum_i \beta_{v,j}\phi_j(v) + \sum_{ij} \beta_{yv,ij}\phi_i(y)\phi_j(v) \quad (5)$$

where the orthogonal basis functions ϕ are nonparametric, spectral, and ordered. GPs of the BSS-ANOVA type support a very broad space of functions,[38] allowing great flexibility for the data-driven determination of the form of the excess free energy function.

The ANOVA decomposition along with the orthogonal and ordered nature of the basis functions in the BSS-ANOVA GP makes possible a data-directed model-building approach, in which a series of models pertaining to different truncations of the expansions in eq 5 are calibrated in a Bayesian sense to a data set. The ordered nature of the basis set facilitates this process: higher-order functions have increased frequency and decreased amplitude.[38,39] The baseline model is representative of the traditional Gouy−Chapman case, where no defect interaction or gradient energy terms are considered. (This is actually a variation of Gouy−Chapman with site exclusion effects: defect concentrations are constrained to the concentration of the corresponding sites at maximum.) With later model versions, defect interactions and gradient energy terms are systematically built into the model structure. Table 1 shows explicitly the effects included in each model version: an X in the corresponding parameter field means that one basis function of the corresponding effect is incorporated into the model, and XX means that two basis functions are incorporated to describe the interaction.

The criterion used to select the optimum model is the "Bayes factor," which is a rigorous statistical metric.[40] Bayes factors balance model fidelity to the data with model

https://dx.doi.org/10.1021/acs.jpcc.0c05713
J. Phys. Chem. C 2020, 124, 23619−23625

Table 1. Table of Model Structures[a]

model	$V_O^{\bullet\bullet}$ segregation	Ca_{Ce}''–Ca_{Ce}''	$V_O^{\bullet\bullet}$–Ca_{Ce}''	$V_O^{\bullet\bullet}$–$V_O^{\bullet\bullet}$	Ca_{Ce}'' gradient	$V_O^{\bullet\bullet}$ gradient
0	X					
1	X	X				
2	X			X		
3	X		X			
4	X	X		X		
5	X		X	X		
6	X	X	X			
7	X	XX	X	X		
8	X	XX	X	XX		
9	X	X	X	XX		
10	X	X			X	
11	X			X		X
12	X	X	X	X		
13	X	X		X	X	
14	X	X		X		X
15	X	X	X		X	
16	X		X	X		X
17	X	X		X	X	X
18	X	X	X	X	X	
19	X	X	X	X		X
20	X	X	X	X	X	X
21	X	XX	X		X	
22	X	XX	X	XX	X	X
23	X	XX	X	XX	XX	XX
24	X	XX	XX	XX	XX	XX

[a]Each X represents one basis function in the GP expansion for the corresponding effect appearing in the excess free energy function.

complexity—generally speaking, the simplest model (i.e., the model with the least number of terms in the GP) that fits the data well will score the highest Bayes factor. The parameter distributions for each model are obtained via Bayesian model calibration[41] using Markov chain Monte Carlo sampling,[42] which yields for each model a joint probability density on the space of the model parameters (called the "posterior distribution"). See the Supporting Information for details on Bayesian calibration and Bayes factors.

RESULTS

A total of 24 models were calibrated to high-spatial-resolution compositional data using the EELS–STEM system (see Supporting Information) gathered from calcium-doped ceria samples with 2, 5, and 10% bulk solute concentration. These experimental data included multiple line scan measurements taken across grain boundaries in each sample and are statistically representative of grain boundaries' composition.[29]

A plot of log Bayes factors versus model number appears in Figure 1. The data-selected model is the model for which the Bayes factor achieves its maximum: model 22. This model includes both local and gradient interaction terms for both dopant cations and vacancies. The means and standard deviations for each model parameter appear in Table 2.

Figure 2 shows model correspondence to the data for model 22 (b) and the baseline model 0 (a), which contains no defect interactions and thus corresponds to a Gouy–Chapman approach[15] with site limitations. The figures were produced by taking 50 samples from the posterior distribution for each model and plotting each (translucent blue lines) on the same figure with the experimental data (multiple-colored solid lines).

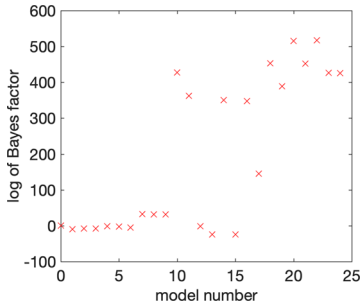

Figure 1. Natural logarithms of the Bayes factor for model versions 0–24.

Figure 3 shows calculations, using a draw of 50 profiles from the posterior distribution, of the concentration of oxygen vacancies as a function of distance from the grain boundary. The model shows the accumulation of positively charged vacancies at the interface, colocated with the accumulation of negatively charged dopants within the space-charge region.

Figure 4 shows the electrostatic potential distribution for a draw of 50 profiles from the posterior distribution for model 22. Space-charge potentials lie between approximately 0.4 and 0.5 V for each concentration studied, and show in each case a crossover region of negative potential at a distance of approximately 1 nm from the interface, indicating a region of charge inversion (i.e., accumulation of positive as opposed to negative charge) related to the coaccumulation of defects as indicated in Figure 3. The fact that potential profiles are relatively unchanged (certainly with respect to dilute-case models) over the compositions studied is largely a consequence of the coaccumulation of oppositely charged defects, which keeps overall charge densities relatively stable. This in turn is a reflection of the fact that in concentrated systems it is chemical interactions more than electrostatic interactions that govern space-charge structure.

DISCUSSION

Inverse Problems and Stochastic Phase-Field Methodology. While first-principles approaches are critical to our understanding of material fundamentals, there are still significant limitations especially when dealing with complex systems. Grain boundaries, nanoparticles, compositional heterogeneities, and dynamic structural modifications are examples where complexity makes it difficult or impractical to describe the system exclusively using ab initio methods. Moreover, many material quantities may not be easily directly observable in experiments. The limitation may be addressed by developing scientifically robust phenomenological approaches, such as the PC-based models utilized in this study, that can be quantitatively trained to experimental observations. Furthermore, the Bayesian approach to the model-based interpretation of data enables the quantitative incorporation of ab initio information in the analysis when it is available.[43]

Despite its early success, the PC method has been criticized for its phenomenological nature—for example, Gregori et al., stated that the parameters appearing in the model formulation of ref 9 "have not been derived from a fundamental theoretical treatment, but adjusted as fit parameter[s] to match the experimental dopant dependence of the bulk conductivity."[10] Most continuum approaches to thermodynamics beyond the

https://dx.doi.org/10.1021/acs.jpcc.0c05713
J. Phys. Chem. C 2020, 124, 23619–23625

Table 2. Model Parameter Statistics[a,b]

$n_o \times 10^5$ (mol/m^2)		f_y (eV)		f_{yv} (eV)		f_v(eV)		c_y(eV nm^2)		c_v(eV nm^2)	
μ	σ	μ	σ	μ	σ	μ	σ	μ	σ	μ	σ
2.02	0.05	0.55	0.25	−0.44	0.27	0.55	0.25	0.46	0.10	0.58	0.15
		0.63	0.24			0.59	0.25				

[a]Split cells indicate that there are two terms in the expansion. [b]n_o is the number of oxygen sites in the core, *f_y is the interaction energy of dopants, f_{yv} is the two-way interaction for oxygen vacancies and dopants, f_v is the interaction energy for oxygen vacancies, c_y is the gradient energy coefficient for dopants, and c_v is the gradient energy coefficient for oxygen vacancies.

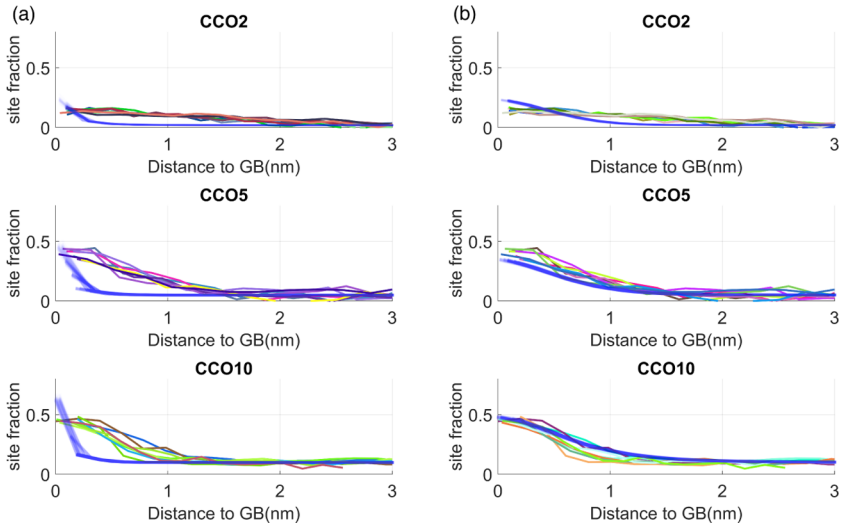

Figure 2. Calibration results for (a) the baseline model and (b) the data-selected model. Each plot shows the site fraction of dopant Ca^{2+} ions as a function of distance to the grain boundary for 2, 5, and 10% bulk calcium concentration. The colored curves represent experimental observations and the group of blue transparent curves represents 50 profiles calculated via model evaluations using samples from the posterior distributions for models 0 and 22.

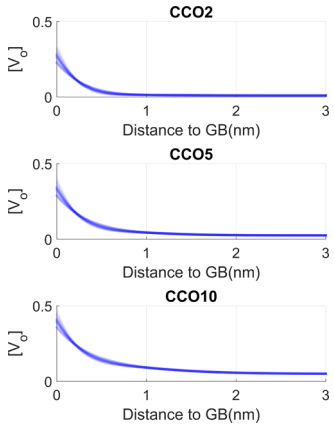

Figure 3. Oxygen vacancy site fraction as a function of distance to the grain boundary for 2, 5, and 10% bulk calcium concentration. The group of curves represents 50 profiles calculated via model evaluations using samples from the posterior distribution for model 22.

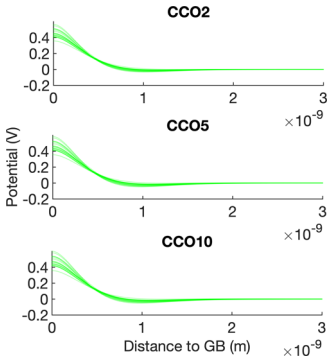

Figure 4. Electrostatic potential as a function of distance to the grain boundary for 2, 5, and 10% bulk calcium concentration. The group of curves represents 50 profiles calculated via model evaluations using samples from the posterior distribution for model 22.

strictly dilute are phenomenological of necessity, as closed-form representations of the partition function are not available except in a small number of cases. However, the fact that a model is phenomenological does not mean that it is unphysical: indeed, these free energy functions can be thought of as measurements made from the experimental data, as previously demonstrated.[44]

The use of models to interpret data sets to estimate physical parameters has a long history in computational science; the practice is usually described among applied mathematicians as "inverse problems."[45−47] Practitioners of inverse problem methodologies use sophisticated methods to quantitatively answer questions using data that may have only an indirect relationship to the parameters of interest. For instance, in the present study, we make quantitative inferences about anion concentrations, even though there is no direct anion data, since oxygen vacancies and calcium dopants are correlated in the free energy functional. Among inverse problem methodologies, Bayesian inverse problems (also called "Bayesian calibration") have proven to be particularly powerful,[48] since the Bayesian perspective simplifies the process of quantifying uncertainty regarding estimated model parameters: if there is insufficient

https://dx.doi.org/10.1021/acs.jpcc.0c05713
J. Phys. Chem. C 2020, 124, 23619−23625

information in the data to estimate model parameters, this will be reflected in the corresponding joint posterior probability distribution obtained through Bayesian calibration.

The method of data-driven model building using GP stochastic functions to represent uncertain functionalities in continuum model forms is a recent development in the field of Bayesian calibration.[49−52] The application to phase-field modeling is a novel aspect of the current work. Phase-field modeling is an excellent candidate for a data-driven approach, as it is a physical, continuum-scale approach that requires thermodynamic functional forms that are known only approximately. The "stochastic phase-field" method reported here can obtain continuum functional forms from experimental or first-principles theoretical (quantum and atomistic) data sets.

Properties of the Model Specified by the Data. *Performance Against Poisson−Boltzmann Model Forms.* Figures 1 and 2 show that the Poisson−Cahn model clearly outperforms the Gouy−Chapman baseline. The posterior odds that model 22 is the model that produced the data versus the baseline (model 0) are 10^{217}-to-1. The enormity of this number is due to the fact that this is a ratio of probability densities on a high-dimensional data space, but in any event, this is high enough to establish the statistical significance of the conclusion that the model with gradient energy terms far outperforms the Gouy−Chapman model for this microscopic data set. Note also that all models with local interaction terms but no gradient terms (models 1−9) perform significantly worse against the data set than the models with gradient terms, showing that an inhomogeneous thermodynamic approach is required to successfully model the data.

Correspondence to Data. The correspondence of the selected model to the data is excellent for the two higher concentrations, while the 2% concentration displays some residual model error. It is possible that this could be resolved by the introduction of a bound electron, such as Ce^{3+}. Such a species would exist only in very low bulk concentrations for the experimental conditions studied, but those concentrations would increase in the vicinity of the interface and would be highest for the lowest dopant concentrations. Impurities, which have recently been found in significant concentrations at grain boundaries in doped ceria[53]—could also potentially explain the residual error. The influence of Ce^{3+} and potentially impurities on space-charge zones in acceptor-doped ceria electrolytes will be explored in future studies.

Co-accumulation. The space-charge region in many oxygen-conducting ceramics forms when oxygen vacancies segregate to the grain boundary core. In dilute systems, this results in a depletion of oxygen vacancies (and corresponding enrichment of oppositely charged species) in the space-charge region due to long-range electrostatic forces.[7,8,10] The observed co-accumulation of oppositely charged defects at grain boundaries in neodymium-doped ceria via atom probe tomography[25] was thus a striking addendum to the growing body of experiments showing that space-charge layers in ceramics are not governed solely by long-range electrostatic forces and Boltzmann statistics. (Co-accumulation in doped ceria had been previously predicted in atomistic simulations.[26]) Figure 3 shows that the extent of the co-accumulation region shrinks as the bulk dopant concentration decreases, suggesting that the expected depletion zone for vacancies will appear at dilute concentrations, as has been shown for applications of the Poisson−Cahn framework in other systems.[9] We emphasize that co-accumulation is only possible in a continuum theory that includes gradient effects or other inhomogeneous thermodynamics.

The predicted concentration of oxygen vacancies in the core reaches nearly 40%, which is a high concentration—considerably higher than that measured by Diercks et al. for the neodymium-doped system.[25] However, this concentration is only reached at the grain boundary core and is close to the measured calcium concentrations there. Atomistic simulations show comparably high oxygen vacancy concentrations at surfaces in both gadolinium-doped ceria and yttria-stabilized zirconia, with no change in the crystal structure.[26] This suggests that high vacancy concentrations at or near grain boundary cores are feasible at least in principle.

Parameter Estimates. The estimated values appearing in Table 2 fall generally in the range of calculated values appearing in the literature for interaction energies in acceptor-doped ceria.[54−57] Calculations of gradient energy coefficients exist in the literature only for metals as far as the authors are aware.[58−63,a]

Gradient energy coefficients are theoretically well defined; however, it is difficult to calculate them directly. Precise expressions relating interatomic potentials and gradient energy coefficients have been derived for an Ising lattice[65] and other estimates of gradient energy coefficients have been provided through comparison of the continuum model form with atomistic simulations[62,63] and in at least one case through an approximate closed-form analysis.[59] If excess entropy is ignored, "regular solution" estimates of the coefficients—which are independent of the solute concentration—are available using straightforward lattice summations.[35,60] However, these estimates are only valid in relatively dilute cases; as solute concentrations and interaction energies increase, rigorously estimated gradient energy coefficients may vary strongly with concentration.[62]

CONCLUSIONS

This work reports a data-driven model-building methodology for the phase-field models of the Cahn−Hilliard type appropriate for charged surfaces and interfaces. The new model replicates defect concentration profiles near grain boundaries in calcium-doped ceria as measured by STEM−EELS. It is the only existing continuum theory shown to quantitatively replicate microscopic data for defect concentrations near grain boundaries in solid electrolytes. It is also the only existing continuum theory to show coaccumulation of oxygen vacancies and dopant cations at grain boundaries in acceptor-doped ceria. The inhomogeneous, excess free energy function at the interface was estimated from the data.

ASSOCIATED CONTENT

Supporting Information

The Supporting Information is available free of charge at https://pubs.acs.org/doi/10.1021/acs.jpcc.0c05713.

Detailed description of the methods used in the production of the results (PDF)

AUTHOR INFORMATION

Corresponding Author

David S. Mebane − *Department of Mechanical and Aerospace Engineering, West Virginia University, Morgantown, West*

https://dx.doi.org/10.1021/acs.jpcc.0c05713
J. Phys. Chem. C 2020, 124, 23619−23625

Virginia 26506, United States; orcid.org/0000-0002-2198-7276; Email: david.mebane@mail.wvu.edu

Authors

Xiaorui Tong − *Department of Mechanical and Aerospace Engineering, West Virginia University, Morgantown, West Virginia 26506, United States*

William J. Bowman − *School for the Engineering of Matter, Transport and Energy, Tempe, Arizona 85287, United States;* orcid.org/0000-0002-4346-1144

Alejandro Mejia-Giraldo − *Department of Mechanical and Aerospace Engineering, West Virginia University, Morgantown, West Virginia 26506, United States*

Peter A. Crozier − *School for the Engineering of Matter, Transport and Energy, Tempe, Arizona 85287, United States;* orcid.org/0000-0002-1837-2481

Complete contact information is available at: https://pubs.acs.org/10.1021/acs.jpcc.0c05713

Notes

The authors declare no competing financial interest.

■ ACKNOWLEDGMENTS

X.T., A.M.-G., and D.S.M. were supported by the National Science Foundation (NSF) grant CBET-1705397. W.J.B. and P.A.C. gratefully acknowledge the support of NSF grant DMR-1308085. W.J.B. acknowledges the NSF's Graduate Research Fellowship (DGE-1211230) for financial support. The authors gratefully acknowledge access to the John M. Cowley Center for High-Resolution Electron Microscopy at Arizona State University. The authors thank Angelo Cassiadoro for assistance in preparing the manuscript.

■ ADDITIONAL NOTE

[a]The boundary condition (4) in the supplement contains the product $n_o f_o$, where f_o is the segregation energy of oxygen vacancies to the core. Since only one of these parameters is estimable, f_o was fixed at a value of −2 eV.[64]

■ REFERENCES

(1) Wachsman, E. D.; Lee, K. T. Lowering the temperature of solid oxide fuel cells. *Science* **2011**, *334*, 935−939.

(2) Laguna-Bercero, M. Recent advances in high temperature electrolysis using solid oxide fuel cells: A review. *J. Power Sources* **2012**, *203*, 4−16.

(3) Ma, C.; Chen, K.; Liang, C. D.; Nan, C. W.; Ishikawa, R.; More, K.; Chi, M. F. Atomic-scale origin of the large grain-boundary resistance in perovskite Li-ion-conducting solid electrolytes. *Energy Environ. Sci.* **2014**, *7*, 1638−1642.

(4) Elyassi, B.; Rajabbeigi, N.; Khodadadi, A.; Mohajerzadeh, S.; Sahimi, M. An yttria-doped ceria-based oxygen sensor with solid-state reference. *Sens. Actuators, B* **2004**, *103*, 178−183.

(5) Swallow, J. G.; Kim, J. J.; Maloney, J. M.; Chen, D.; Smith, J. F.; Bishop, S. R.; Tuller, H. L.; Van Vliet, K. J. Dynamic chemical expansion of thin-film non-stoichiometric oxides at extreme temperatures. *Nat. Mater.* **2017**, *16*, 749−754.

(6) Ismail, M.; Ahmed, E.; Rana, A.; Hussain, F.; Talib, I.; Nadeem, M.; Panda, D.; Shah, N. Improved endurance and resistive switching stability in ceria thin films due to charge transfer ability of Al dopant. *ACS Appl. Mater. Interfaces* **2016**, *8*, 6127−6136.

(7) Guo, X.; Waser, R. Electrical properties of the grain boundaries of oxygen ion conductors: Acceptor-doped zirconia and ceria. *Prog. Mater. Sci.* **2006**, *51*, 151−210.

(8) De Souza, R. A. The formation of equilibrium space-charge zones at grain boundaries in the perovskite oxide SrTiO3. *Phys. Chem. Chem. Phys.* **2009**, *11*, 9939−9969.

(9) Mebane, D. S.; De Souza, R. A. A generalised space-charge theory for extended defects in oxygen-ion conducting electrolytes: from dilute to concentrated solid solutions. *Energy Environ. Sci.* **2015**, *8*, 2935−2940.

(10) Gregori, G.; Merkle, R.; Maier, J. Ion conduction and redistribution at grain boundaries in oxide systems. *Prog. Mater. Sci.* **2017**, *89*, 252−305.

(11) Kim, S.; Kim, S.; Khodorov, S.; Maier, J.; Lubomirsky, I. On determining the height of the potential barrier at grain boundaries in ion-conducting oxides. *Phys. Chem. Chem. Phys.* **2016**, *18*, 3023−3031.

(12) Karra, S. V.; Chueh, W. C.; Garcia, E. Electrochemical and Mechanical Effects on Charged Interfaces. *Energy Environ. Sci.* **2018**, *11*, No. 15360.

(13) Tong, X. R.; Mebane, D. S.; De Souza, R. A. Analyzing the grain-boundary resistance of oxide-ion conducting electrolytes: Poisson-Cahn vs Poisson-Boltzmann theories. *J. Am. Ceram. Soc.* **2020**, *103*, 5−22.

(14) Bowman, W. J.; Darbal, A.; Crozier, P. A. Linking macroscopic and nanoscopic ionic conductivity: A semi-empirical framework for characterizing grain boundary conductivity in polycrystalline ceramics. *ACS Appl. Mater. Interfaces* **2020**, *12*, 507−517.

(15) Gouy, M. Sur la constitution de la charge électrique à la surface daun électrolyte. *J. Phys. Theor. Appl.* **1910**, *9*, 457−468.

(16) Lei, Y. Y.; Ito, Y.; Browning, N. D.; Mazanec, T. J. Segregation effects at grain boundaries in fluorite-structured ceramics. *J. Am. Ceram. Soc.* **2002**, *85*, 2359−2363.

(17) Shibata, N.; Oba, F.; Yamamoto, T.; Ikuhara, Y.; Sakuma, T. Atomic structure and solute segregation of a Sigma=3, [110]/111 grain boundary in an yttria-stabilized cubic zirconia bicrystal. *Philos. Mag. Lett.* **2002**, *82*, 393−400.

(18) Kubicek, M.; Limbeck, A.; Fromling, T.; Hutter, H.; Fleig, J. Relationship between Cation Segregation and the Electrochemical Oxygen Reduction Kinetics of $La_{0.6}Sr_{0.4}CoO_{3-\delta}$ Thin Film Electrodes. *J. Electrochem. Soc.* **2011**, *158*, B727−B734.

(19) Browning, N. D.; Klie, R. F.; Lei, Y. Y. Vacancy Segregation at Grain Boundaries in Ceramic Oxides. *Mixed Ionic Electron. Conduct. Perovskites Adv. Energy Syst.* **2004**, *81*, 2015−2025.

(20) Lee, W.; Jung, H. J.; Lee, M. H.; Kim, Y. B.; Park, J. S.; Sinclair, R.; Prinz, F. B. Oxygen Surface Exchange at Grain Boundaries of Oxide Ion Conductors. *Adv. Funct. Mater.* **2012**, *22*, 965−971.

(21) Shirpour, M.; Rahmati, B.; Sigle, W.; van Aken, P. A.; Merkle, R.; Maier, J. Dopant segregation and space charge effects in proton-conducting BaZrO3 perovskites. *J. Phys. Chem. C* **2012**, *116*, 2453−2461.

(22) An, J.; Park, J. S.; Koh, A. L.; Lee, H. B.; Jung, H. J.; Schoonman, J.; Sinclair, R.; Gur, T. M.; Prinz, F. B. Atomic Scale Verification of Oxide-Ion Vacancy Distribution near a Single Grain Boundary in YSZ. *Sci. Rep.* **2013**, *3*, No. 2680.

(23) Bowman, W. J.; Zhu, J.; Sharma, R.; Crozier, P. A. Electrical conductivity and grain boundary composition of Gd-doped and Gd/Pr co-doped ceria. *Solid State Ionics* **2015**, *272*, 9−17.

(24) Lin, Y.; Fang, S.; Su, D.; Brinkman, K. S.; Chen, F. Enhancing grain boundary ionic conductivity in mixed ionic-electronic conductors. *Nat. Commun.* **2015**, *6*, No. 6824.

(25) Diercks, D. R.; Tong, J.; Zhu, H.; Kee, R.; Baure, G.; Nino, J. C.; O'Hayre, R.; Gorman, B. P. Three-dimensional quantification of composition and electrostatic potential at individual grain boundaries in doped ceria. *J. Mater. Chem. A* **2016**, *4*, 5167−5175.

(26) Lee, H. B.; Prinz, F. B.; Cai, W. Atomistic simulations of surface segregation of defects in solid oxide electrolytes. *Acta Mater.* **2010**, *58*, 2197−2206.

(27) Aidhy, D. S.; Zhang, Y. W.; Weber, W. J. Impact of segregation energetics on oxygen conductivity at ionic grain boundaries. *J. Mater. Chem. A* **2014**, *2*, 1704−1709.

(28) Nafsin, N.; Aguiar, A.; Aoki, T.; Thron, A. M.; van Benthem, K.; Castro, R. H. R. Thermodynamics versus kinetics of grain growth control in nanocrystalline zirconia. *Acta Mater.* **2017**, *136*, 224−234.
(29) Bowman, W. J.; Kelly, M. N.; Rohrer, G. S.; Hernandez, C. A.; Crozier, P. A. Enhanced ionic conductivity in electroceramics by nanoscale enrichment of grain boundaries with high solute concentration. *Nanoscale* **2017**, *9*, 17293−17302.
(30) Göbel, M. C.; Gregori, G.; Maier, J. Numerical calculations of space charge layer effects in nanocrystalline ceria. Part I: comparison with the analytical models and derivation of improved analytical solutions. *Phys. Chem. Chem. Phys.* **2014**, *16*, 10214−10231.
(31) Kim, S. Isn't the space-charge potential in ceria-based solid electrolytes largely overestimated. *Phys. Chem. Chem. Phys.* **2016**, *18*, 19787−19791.
(32) Lindman, A.; Bjorheim, T. S.; Wahnstrom, G. *J. Mater. Chem. A* **2017**, *5*, 13421−13429.
(33) de Klerk, N. J. J.; Wagemaker, M. Space-charge layers in all-solid-state batteries: Important or negligible. *ACS Appl. Energy Mater.* **2018**, *1*, 5609−5618.
(34) Brogioli, D.; Langer, F.; Kun, R.; La Mantia, F. Space-charge effects at the $Li_7La_3Zr_2O_{12}$/poly(ethylene oxide) interface. *ACS Appl. Mater. Interfaces* **2019**, *11*, 11999−12007.
(35) Cahn, J. W.; Hilliard, J. E. Free energy of a nonuniform system. I. Interfacial free energy. *J. Chem. Phys.* **1958**, *28*, 258−267.
(36) Mebane, D. S. A variational approach to surface cation segregation in mixed conducting perovskites. *Comput. Mater. Sci.* **2015**, *103*, 231−236.
(37) Zurhelle, A. F.; Tong, X. R.; Klein, A.; Mebane, D. S.; De Souza, R. A. Space-charge treatment of the increased concentration of reactive species at the surface of a ceria solid solution. *Angew. Chem., Int. Ed.* **2017**, *56*, 14516−14520.
(38) Reich, B.; Storlie, C.; Bondell, H. Variable selection in Bayesian smoothing spline ANOVA models: Application to deterministic computer codes. *Technometrics* **2009**, *51*, 110−120.
(39) Storlie, C. B.; Lane, W. A.; Ryan, E. M.; Gattiker, J. R.; Higdon, D. M. Calibration of computational models with categorical parameters and correlated outputs via Bayesian smoothing spline ANOVA. *J. Am. Stat. Assoc.* **2015**, *110*, 68−82.
(40) Kass, R. E.; Raftery, A. E. Bayes factors. *J. Am. Stat. Assoc.* **1995**, *90*, 773−795.
(41) Kennedy, M. C.; O'Hagan, A. Bayesian calibration of computer models. *J. R. Stat. Soc., B* **2001**, *63*, 425−464.
(42) Gilks, W. R.; Richardson, S.; Spiegelhalter, D. *Markov Chain Monte Carlo in Practice*; CRC Press, 1995.
(43) Mebane, D. S.; Bhat, K. S.; Kress, J. D.; Fauth, D. J.; Gray, M. L.; Lee, A.; Miller, D. C. Bayesian calibration of thermodynamic models for the uptake of CO_2 in supported amine sorbents using ab initio priors. *Phys. Chem. Chem. Phys.* **2013**, *15*, 4355−4366.
(44) Ostace, A.; Kocan, K. X.; Mebane, D. S.; Schmal, J. P.; Bhattacharyya, D. Probabilistic model building with uncertainty quantification and propagation for a dynamic fixed bed CO_2 capture process. *Energy Fuels* **2020**, *34*, 2516−2532.
(45) Yeh, W. W. G. Review of parameter-identification procedures In groundwater hydrology - The inverse problem. *Water Resour. Res.* **1986**, *22*, 95−108.
(46) Borcea, L. Electrical impedance tomography. *Inverse Probl.* **2002**, *18*, 99−136.
(47) Avril, S.; Bonnet, M.; Bretelle, A. S.; Grediac, M.; Hild, F.; Ienny, P.; Latourte, F.; Lemosse, D.; Pagano, S.; Pagnacco, E.; Pierron, F. Overview of identification methods of mechanical parameters based on full-field measurements. *Exp. Mech.* **2008**, *48*, 381−402.
(48) Stuart, A. M. Inverse problems: A Bayesian perspective. *Acta Numer.* **2010**, *19*, 451−559.
(49) Sargsyan, K.; Najm, H. N.; Ghanem, R. On the statistical calibration of physical models. *Int. J. Chem. Kinet.* **2015**, *47*, 246−276.
(50) Bhat, K. S.; Mebane, D. S.; Mahapatra, P.; Storlie, C. B. Upscaling uncertainty with dynamic discrepancy for a multi-scale carbon capture system. *J. Am. Stat. Assoc.* **2017**, *112*, 1453−1467.
(51) Li, K. J.; Mahapatra, P.; Bhat, K. S.; Miller, D. C.; Mebane, D. S. Multi-scale modeling of an amine sorbent fluidized bed adsorber with dynamic discrepancy reduced modeling. *React. Chem. Eng.* **2017**, *2*, 550−560.
(52) Lei, Y. K.; Chen, T. L.; Mebane, D. S.; Wen, Y. H. Reduced-order model for microstructure evolution prediction in the electrodes of solid oxide fuel cell with dynamic discrepancy reduced modeling. *J. Power Sources* **2019**, *416*, 37−49.
(53) Xu, X.; Liu, Y. Z.; Wang, J.; Isheim, D.; Dravid, V. P.; Phatak, C.; Haile, S. M. Variability and origins of grain boundary electric potential detected by electron holography and atom probe tomography. *Nat. Mater.* **2020**, *19*, 887−893.
(54) Gerhardt-Anderson, R.; Nowick, A. Ionic conductivity of CeO_2 with trivalent dopants of different ionic radii. *Solid State Ionics* **1981**, *5*, 547−550.
(55) Wang, D. Y.; Park, D. S.; Griffith, J.; Nowick, A. S. Oxygen-ion conductivity and defect interactions in yttria-doped ceria. *Solid State Ionics* **1981**, *2*, 95−105.
(56) Grieshammer, S.; Grope, B. O.; Koettgen, J.; Martin, M. A combined DFT+ U and Monte Carlo study on rare earth doped ceria. *Phys. Chem. Chem. Phys.* **2014**, *16*, 9974−9986.
(57) Nakayama, M.; Martin, M. First-principles study on defect chemistry and migration of oxide ions in ceria doped with rare-earth cations. *Phys. Chem. Chem. Phys.* **2009**, *11*, 3241−3249.
(58) Han, B.; Van der Ven, A.; Morgan, D.; Ceder, G. Electrochemical modeling of intercalation processes with phase field models. *Electrochim. Acta* **2004**, *49*, 4691−4699.
(59) Liu, Z. R.; Gao, H. A differential cluster variation method for analysis of spinodal decomposition in alloys. *Eur. Phys. J. B* **2004**, *37*, 369−374.
(60) Lass, E. A.; Johnson, W. C.; Shiflet, G. J. Correlation between CALPHAD data and the Cahn-Hilliard gradient energy coefficient κ and exploration into its composition dependence. *Calphad* **2006**, *30*, 42−52.
(61) Rundman, K.; Hilliard, J. Early stages of spinodal decomposition in an aluminum-zinc alloy. *Acta Metall.* **1967**, *15*, 1025−1033.
(62) Asta, M.; Hoyt, J. Thermodynamic properties of coherent interfaces in FCC-based Ag-Al alloys: A first-principles study. *Acta Mater.* **2000**, *48*, 1089−1096.
(63) Hoyt, J. Molecular dynamics study of equilibrium concentration profiles and the gradient energy coefficient in Cu-Pb nanodroplets. *Phys. Rev. B: Condens. Matter Mater. Phys.* **2007**, *76*, No. 094102.
(64) Tschöpe, A.; Kilassonia, S.; Birringer, R. The grain boundary effect in heavily doped cerium oxide. *Solid State Ionics* **2004**, *173*, 57−61.
(65) Binder, K.; Frisch, H. Dynamics of surface enrichment: A theory based on the Kawasaki spin-exchange model in the presence of a wall. *Z. Phys. B: Condens. Matter* **1991**, *84*, 403−418.

https://dx.doi.org/10.1021/acs.jpcc.0c05713
J. Phys. Chem. C 2020, 124, 23619−23625

A New Data-Driven Interacting-Defect Model Describing Nanoscopic Grain Boundary Compositions in Ceramics

Supplementary Information

Xiaorui Tong,[†] William J. Bowman,[‡,¶] Alejandro Mejia-Giraldo,[†] Peter A. Crozier,[‡] and David S. Mebane[*,†]

[†]*Department of Mechanical and Aerospace Engineering, West Virginia University, Morgantown, WV, USA*

[‡]*School for the Engineering of Matter, Transport and Energy, Tempe, Arizona, USA*

[¶]*Current address: Department of Materials Science and Engineering, University of California at Irvine, Irvine, CA, USA*

E-mail: david.mebane@mail.wvu.edu

Euler-Lagrange Equations

Variational analysis of the functional (1) in the main text combined with equations (4) and (5) yields the Euler-Lagrange equations (assuming a one-dimensional domain with the grain boundary core at $x = 0$):

$$\begin{aligned} 2n_{\mathrm{os}}F\varphi + n_{\mathrm{os}}RT\log\frac{v}{1-v} + \sum_i \beta_{\mathrm{v}i}\phi_i'(v) - 2\beta^0_{\mathrm{v}'i}\frac{d^2v}{dx^2} + \sum_i \beta_{\mathrm{v}'i}\phi_i'(v)(\frac{dv}{dx})^2 \\ - \sum_i \beta_{\mathrm{v}'i}\phi_i'(v)2\frac{dv}{dx} - \sum_i \beta_{\mathrm{v}'i}\phi_i(v)2\frac{d^2v}{dx^2} + \sum_i \beta_{\mathrm{vy}i}\phi_i'(v)\phi_i(y) \\ + \lambda_v = 0 \end{aligned} \tag{1}$$

$$\begin{aligned} -2n_{\mathrm{cs}}F\varphi + n_{\mathrm{cs}}RT\log\frac{y}{1-y} + \sum_i \beta_{\mathrm{y}i}\phi_i'(y) - 2\beta^0_{\mathrm{y}'i}\frac{d^2y}{dx^2} + \sum_i \beta_{\mathrm{y}'i}\phi_i'(y)(\frac{dy}{dx})^2 \\ - \sum_i \beta_{\mathrm{y}'i}\phi_i'(y)2\frac{dy}{dx} - \sum_i \beta_{\mathrm{y}'i}\phi_i(y)2\frac{d^2y}{dx^2} + \sum_i \beta_{\mathrm{vy}i}\phi_i'(y)\phi_i(v) \\ + \lambda_y = 0 \end{aligned} \tag{2}$$

$$\varepsilon_r\varepsilon_0\frac{d^2\varphi}{dx^2} + F(2n_{os}v - 2n_{cs}y) = 0 \tag{3}$$

Natural boundary conditions at the grain boundary core assume a simple, linear segregation energy for oxygen vacancies (f_{o}) relative to the bulk, and no segregation of dopants:

$$2\beta^0_{\mathrm{v}'i}\frac{dv}{dx}\Big|_{x=0} + \sum_i \beta_{\mathrm{v}'i}\phi_i(v)2\frac{dv}{dx}\Big|_{x=0} = n_{\mathrm{o}}f_{\mathrm{o}} \tag{4}$$

$$2\beta^0_{\mathrm{y}'i}\frac{dy}{dx}\Big|_{x=0} + \sum_i \beta_{\mathrm{y}'i}\phi_i(y)2\frac{dy}{dx}\Big|_{x=0} = 0 \tag{5}$$

$$\frac{d\varphi}{dx}\Big|_0 = 0 \tag{6}$$

where n_{o} is the site density for oxygen in the core.

The equations were discretized using adaptive finite elements with linear basis functions, and the resulting system of algebraic equations were solved using Newton's method. The

solver was implemented in MATLAB.

Data-Driven Model Building

A series of models pertaining to the model form (6)-(11) in the main text arise from a steady increase in the number of basis functions used in the expansion (3). The basis functions are orthogonal, spectral, nonparametric and ordered: higher order functions have increased frequency and decreased amplitude.[1,2] The baseline model is representative of the traditional Gouy-Chapman case, where no defect interaction or gradient energy terms are considered. (Site exclusion is included.) With later model versions, defect interactions and gradient energy terms are systematically built into the model structure, as shown in Table 1.

Using the experimentally-derived Ca profiles near GBs in 2, 5 and 10% Ca-doped CeO_2, Bayesian calibration is employed in order to identify parameter posterior distributions for each model. A Bayesian approach to parameter estimation treats parameters as random variables, quantified in terms of a joint probability distribution on the multi-dimensional parameter space. Prior probability distributions for the parameters are updated with the data *via* Bayes' theorem, to yield the posterior distribution for the parameters in light of the data:

$$\mathcal{P}(\theta|Z) = \frac{\pi(\theta)\mathcal{L}(Z|\theta)}{\int_{\theta'} \pi(\theta')\mathcal{L}(Z|\theta')} \tag{7}$$

Here Z is the vector of experimental data, θ is the parameter vector, $\mathcal{P}(\theta|Z)$ is the posterior distribution, $\pi(\theta)$ is the prior distribution, and $\mathcal{L}(Z|\theta)$ is the likelihood, which includes both the physical model and a model for the observation error of the experiment. The denominator on the right-hand side is the integrated probability of observing Z over the entire parameter space, or the evidence for the associated model, which is used in the calculation of Bayes factors (discussed below).

Because the denominator on the right-hand side of (7) is not analytical, the posterior distribution $\mathcal{P}$ must be obtained numerically. A commonly-used tool is the Markov chain Monte

Carlo (MCMC) sampler.[3,4] MCMC samplers simulate a sample from the target distribution (in this case, $\mathcal{P}$) by walking through the parameter space, proposing a new sample point in proximity to the most recently recorded point, and accepting or rejecting the proposal based on a comparison of the numerator of (7) evaluated at the proposal to the same product evaluated at the most recently recorded point. The procedure is guaranteed to converge to the target distribution in the limit of infinite sampling time; in practice (of course) the procedure must be truncated at some point. Sampling efficiency and convergence criteria (unlike the case of the infinite sample, convergence to the target of a truncated routine can never be absolutely guaranteed) are thus critical aspects of MCMC samplers. The sampler employed in this study was the adaptive proposal type, meaning that the proposal changes as the routine moves forward in order to obtain greater sampling efficiency. The covariance matrix was the 'moving window'type was updated every 2000 MCMC steps. An adjustable multiplier is used with the covariance matrix to deal with out-of-bounds proposals and to achieve a reasonable acceptance rate. The MCMC process continues until the criteria for posterior distribution convergence is satisfied. A Student's T-test on batch means with a 95% confidence interval is used to test the convergence: the convergence target of $\pm 5\%$ or less of the sampled mean for each estimated parameter was met for all calibrations.

Model Comparison Using Bayes Factors

Bayes factors constitute a method of hypothesis testing via a ratio of the evidences of two competing models:

$$B_{12} = \frac{\int \mathcal{L}_1(Z|\theta_1)\pi_1(\theta_1)d\theta_1}{\int \mathcal{L}_2(Z|\theta_2)\pi_2(\theta_2)d\theta_2} \tag{8}$$

The Bayes factor is a metric that is easy to interpret for data-driven model building, as the evidence for a given model can be viewed as a probability that the model produced the calibration data. Used as a model fitness criterion, it naturally strikes a balance between fidelity to the data and overfitting.

Calculating the evidence (and thus the Bayes factor) is a difficult undertaking, especially for high-dimensional models. A first-order estimate may be obtained through the Laplace method, which fits a Gaussian distribution to the posterior sample obtained by the MCMC routine and takes the mode of that distribution as an estimate of the posterior density at that point – equation (7) then enables an estimate of the evidence.[5] A related and possibly more accurate method uses kernel smoothing to fit a density to the entire posterior sample, yielding an estimate for the density at every sampled point. We used the kernel density estimation routine 'akde', which uses a diffusion model to select the optimal bandwidth.[6] This yielded a set of estimates for the evidence, from which a mean value was extracted. Bounding procedures such as those discussed in Ref. 5 were explored; it was found that they did not appreciably change the estimates obtained when including every point in the sample.

Electron Energy Loss Spectroscopy

Calcium concentration profiles near grain boundaries in $Ca_xCe_{1-x}O_{2-x}$ measured using electron energy-loss spectroscopy (EELS) for three different nominal concentrations with $x = 0.02, 0.05, 0.1$[7] were utilized for model building and validation. In later context, the profiles pertain to three different concentrations denoted CCO2, CCO5 and CCO10, respectively. For computational use, profiles around the two sides of the GB are treated as two separate datasets. EELS data were acquired using a JEOL ARM 200F aberration-corrected scanning transmission electron microscope (STEM) equipped with a Gatan Enfina spectrometer; full experimental details are published in Ref. 7.

References

(1) Reich, B., Storlie, C. & Bondell, H. Variable selection in bayesian smoothing spline anova models: Application to deterministic computer codes. *Technometrics* **51**, 110–120 (2009).

(2) Storlie, C. B., Lane, W. A., Ryan, E. M., Gattiker, J. R. & Higdon, D. M. Calibration of computational models with categorical parameters and correlated outputs via bayesian smoothing spline anova. *Journal of the American Statistical Association* **110**, 68–82 (2015).

(3) Hastings, W. K. Monte carlo sampling methods using markov chains and their applications. *Biometrika* **57**, 97–109 (1970).

(4) Gilks, W. R., Richardson, S. & Spiegelhalter, D. *Markov chain Monte Carlo in practice* (CRC press, 1995).

(5) DiCiccio, T. J., Kass, R. E., Raftery, A. & Wasserman, L. Computing bayes factors by combining simulation and asymptotic approximations. *Journal of the American Statistical Association* **92**, 903–915 (1997).

(6) Botev, Z. I., Grotowski, J. F. & Kroese, D. P. Kernel density estimation via diffusion. *Annals of Statistics* **38**, 2916–2957 (2010).

(7) Bowman, W. J., Kelly, M. N., Rohrer, G. S., Hernandez, C. A. & Crozier, P. A. Enhanced ionic conductivity in electroceramics by nanoscale enrichment of grain boundaries with high solute concentration. *Nanoscale* **9**, 17293–17302 (2017).